since 1961

Baltica

BALTICA Volume 38 Number 2 December 2025: 209–224
https://doi.org/10.5200/baltica.2025.2.8

Lithospheric structure of the Aegean region from simultaneous inversion of P- and S-receiver functions: results from the records of different band types

Hamdi Alkan

Alkan, H. 2025. Lithospheric structure of the Aegean region from simultaneous inversion of P- and S-receiver functions: results from the records of different band types. *Baltica 38 (2)*, 209–224. Vilnius. ISSN 1648-858X.
Manuscript submitted 18 June 2025 /Accepted 5 December 2025 / Available online 19 December 2025

Abstract. The Aegean region is a key component of the Eastern Mediterranean basin and covers the subduction of the African Lithospheric Plate beneath the Aegean along the Hellenic Arc and the western movement of the Anatolian Plate. In this research, simultaneous inversion of teleseismic P- and S-Receiver Functions (RFs) is used to investigate the crust and upper mantle structure of the Aegean region. For this purpose, data from the different band-type seismic stations arranged along the Hellenic Arc are used to calculate receiver functions. The study involves 452 P-Receiver Functions and 237 S-Receiver Functions from 8 stations. Although the seismic stations are nearby, the S-wave velocity models in the south and north turn out to have different structural discontinuities. Also, the results of stacking P-Receiver Functions indicate the significant *Ps* and *Sp* phases from the Aegean Moho and the African Slab. The Moho depth of the African Slab along the Hellenic Arc ranges from 45 to 56 km, with an average crustal shear wave velocity of Vs = 4.5 km/s. The lithosphere-asthenosphere boundary (LAB) is observed at depths of approximately 155 km around the Hellenic Arc and corresponds to the subduction of the African Slab. However, the LAB depths of the eastern and western stations are consistent with the Anatolian and mainland Greece. Finally, these observations can be interpreted as part of the African subduction system and the Anatolian lithospheric system in the study region.

Keywords: *Aegean Sea; receiver function; joint inversion; Moho; lithosphere-asthenosphere boundary (LAB)*

Hamdi Alkan (hamdialkan@yyu.edu.tr), https://orcid.org/0000-0003-3912-7503
Department of Geophysics, Van Yüzüncü Yıl University, 65080, Van, Türkiye

INTRODUCTION

The Aegean region, as a part of the Eastern Mediterranean basin, includes the Aegean Sea in the centre, western Anatolia in the east, the island of Crete in the south, and the continental Greece complex and Ionian Sea in the west. The region has undergone collision mechanisms due to the northward subduction of the African Oceanic Plate along the Hellenic-Cyprus Arcs convergent boundary at a rate of ~ 10 mm/yr under the Eurasian Plate from the late Cretaceous to the Eocene, and the Arabian-Eurasian convergence and the displacement of the Anatolian-Aegean microplate (McKenzie 1972; Li *et al.* 2003; Sodoudi *et al.* 2006; Zhu *et al.* 2006; Di Luccio, Pasyanos 2007; Öztürk, Alkan 2024; Mulumulu *et al.* 2025). The convergent plate boundary forms the Hellenic Arc, which is characterized by high seismic activity and may contribute to the rotation of the Anatolian-Aegean Plates (Sodoudi *et al.* 2015). According to plate motion slip rates, the westward migration of the Anatolian Plate at a rate of ~ 20 mm/yr has resulted in significant deformation in the eastern part of the Aegean Sea (Fig. 1a). This westward movement has led to the rollback of the subducting African lithosphere, resulting in a relative displacement of approximately 30 mm/yr in the SW direction along the Hellenic subduction zone (McClusky *et al.* 2000; Reilinger *et al.* 2006). On the other hand, the relative motion of the right-lateral north Anatolian fault from east to west at a rate of 20–25 mm/yr has played a significant role in controlling crustal deformation and Aegean active geodynamics (Drymoni *et al.* 2022; Tamtas, Toktay 2025).

The Aegean region has strong seismic activity both

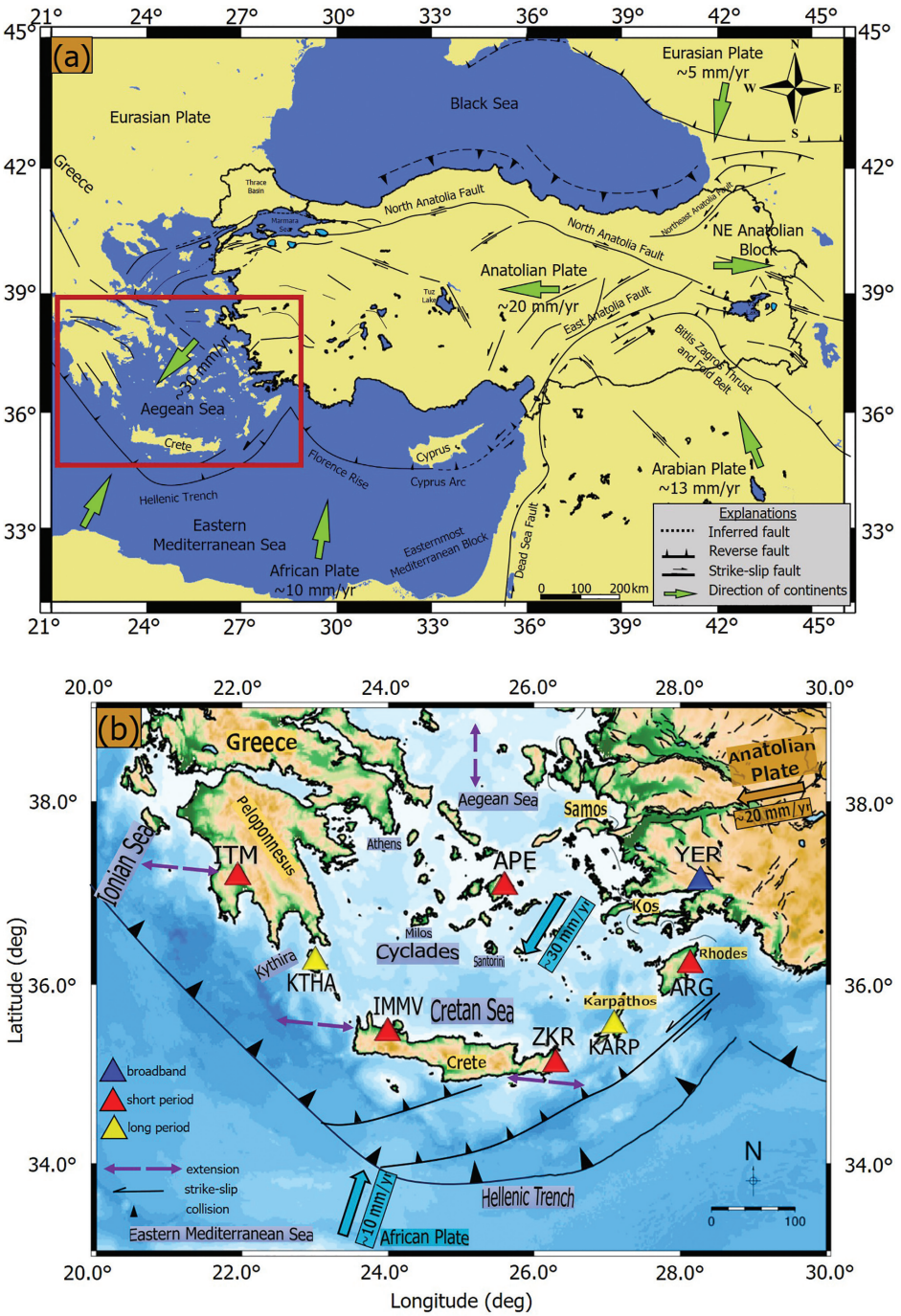

Fig. 1 (a) The main tectonic structures of the Eastern Mediterranean region modified from Bozkurt (2001), Reilinger *et al.* (2006), Emre *et al.* (2018), and Alkan *et al.* (2021). The red square represents the study region. **(b)** Maintopographic features of tectonic origin of the Aegean region, compiled from Bozkurt (2001), Di Luccio and Pasyanos (2007), Sachpazi *et al.* (2016), Kassaras *et al.* (2020), and Drymoni *et al.* (2022). Fault lines are taken from Emre *et al.* (2018) and Makris *et al.* (2022). Grey and blue arrows represent plate motions (McClusky *et al.*2000). Blue, red, and yellow triangles denote the locations of seismic stations

inland and offshore in the instrumental and historical periods. Generally, moderate to strong earthquakes in the past with various focal mechanisms, such as strike-slip, normal, and reverse faults, occur at shallow to intermediate crustal depths and in the upper mantle along convergent plate boundaries. The seismicity is primarily concentrated along the Hellenic Volcanic Arc, western Anatolia, and the Cyclades region (Di Luccio, Pasyanos 2007; Yolsal-Çevikbilen, Taymaz 2012). The largest earthquakes in the Aegean region occurred in 1956 with magnitudes of M_S = 7.4 and M_S = 7.2, the 2017 Kos earthquake (M_W = 6.6), and the 2020 Samos earthquake (M_W = 7.0) in the instrumental time (Bohnhoff *et al.* 2006; Sardeli *et al.* 2023). Also, Crete Island, located on the Hellenic subduction zone, is an important region because of

the subduction of the African lithosphere beneath the Aegean lithosphere (Meier *et al.* 2004). In this region, the scientist defined a Benioff zone of the Hellenic subduction zone at a depth of 150 to 200 km, occurring deeper earthquakes occur along the subduction zones (Papazachos *et al.* 2000; Meier *et al.* 2004; Karagianni *et al.* 2005; Dimitriadis *et al.* 2009). The subslab hot mantle upwelling beneath the subducting Hellenic Slab, an extensive volcanic eruption in the Aegean Sea, might be fuelled by a mixture of island arc magma (Toyokuni, Zhao 2025). Due to the complex mechanisms, the Aegean volcanic arc occurred along the north of the Hellenic trench and is a characteristic feature of the back-arc basin of the Hellenic Arc, which experiences earthquake swarms in some periods, which took place recently in 2011–2012 and 2025 in the Santorini volcanic complex (Sardeli *et al.* 2023; Papathoma-Köhle 2025).

Due to the complex mantle dynamics and high seismicity, the crustal and upper mantle structures of the Aegean region and its surroundings are investigated with all kinds of seismological studies, including seismic tomography, gravity data, receiver function, and seismic refraction to understand lithospheric dynamics and crustal structures (Endrun *et al.* 2011; Yolsal-Çevikbilen, Taymaz 2012; Gönenç, Akgün 2012; Faccenna *et al.* 2014; Cosette *et al.* 2016; Evangelidis 2017; Dogru *et al.* 2018; Briole *et al.* 2021). According to Li *et al.* (2003), the oceanic Moho discontinuity of the subducted African Plate was observed at approximately 56 km beneath Gavdos and Crete islands, while this boundary was observed nearly 100 km beneath Santorini Island. Based on gravity inversion, Tirel *et al.* (2004) provided insights into the geodynamic structure of the Aegean, naming three distinct provinces: the north Aegean, the Cyclades, and the Cretan Sea. Zhu *et al*. (2006) demonstrated the crustal thinning from 36 km beneath western Anatolia to about 25 km beneath the Cycladic massif in the middle of the Aegean Sea. Sodoudi *et al.* (2006, 2015) studied the lithospheric structures of the Aegean using receiver function analysis, focusing on the subducted African Plate from south to north. The Moho of the subducting African Plate was seen at a shallow depth in the southern part of the Aegean Sea, while it was found at a greater depth in the northern part of the Aegean Sea. Di Luccio and Pasyanos (2007), using group velocity dispersion curves, detected the thick sediments beneath the eastern Mediterranean and the Hellenic subduction zone. They found the low-velocity zones in the upper mantle of the Crete Island, associated with serpentinized mantle from the subducting African lithosphere. High-resolution tomographic images revealed that the south-westernmost termination of the low-velocity anomaly corresponds to the northward-dipping Hellenic Slab below the Aegean region (Salaün *et al.* 2012). Beneath the Cyclades metamorphic core complex, in the central part of the Aegean Sea, the velocity structure of the crust and sediments was investigated by Makris *et al.* (2022). Karabulut *et al.* (2019) combined the high-resolution seismic data and Bouguer gravity anomaly data to interpret the crust and lithospheric mantle structure beneath the Anatolia-Aegean domain. They proposed a thin crust, low elevations beneath the Aegean Sea. From ambient noise tomography, Mulumulu *et al.* (2025) found narrow anticlines and basin-type wide synclines and sedimentary layers. These variations look like offshore geothermal zones and hot fluid contents.

To infer the lithospheric structure in the Aegean region, the published teleseismic receiver function studies that mapped *S*-wave velocities are generally used to analyze waveforms from the same type of stations, such as broadband or long-period stations. On the contrary, in this study, the lithospheric structure of the Aegean region up to 300 km is investigated using data from stations with different band types, including broadband, short-period, and long-period data. Therefore, the main aim of this study is to image the detailed *S*-wave models of crustal and upper mantle discontinuities beneath the Aegean Sea from the simultaneous inversion of the P- and S-Receiver Functions (PRFs and SRFs, respectively) with teleseismic P- and S-travel time residuals (Farra, Vinnik 2000; Oreshin *et al.* 2002, 2008, 2011; Kosarev *et al.* 2013; Vinnik *et al.* 2009, 2016). The joint inversion algorithm is obtained with high resolution to understand the deep structure in detail, which helps to provide better constraints than separate inversions.

DATA FOR P- AND S-RECEIVER FUNCTIONS

In this study, 8 seismic stations make up one broadband, two long-period, and five short-period stations located on Peloponnesus, Crete, Karpathos, Rhodes, Anatolia, and Naxos (Fig. 1b). Station names include KTHA, IMMV, ZKR, KARP, ARG, YER, APE, and ITM. The geographical coordinates, starting times, and sensor models of the seismic stations are provided in Table 1. Data from all stations were sourced from the EIDA data archive (https://www.orfeus-eu.org/data/eida/). The stations ZKR, KTHA, KARP, IMMV, and APE are operated by the GEOFON seismic network; ITM and ARG are part of the Hellenic seismic network; YER is maintained by the Kandilli Observatory and Earthquake Research Institute (KOERI). All raw data were gathered from 2005 to 2024. For PRFs, teleseismic events were selected with epicentral distances ranging from 30° to 90°. For SRFs, teleseismic events were chosen with epicentral distances between 65° and 90°. These epicentral dis-

tances are selected because of association with relatively *P*-to-*S* (*Ps*) and *S*-to-*P* (*Sp*) conversions from crust and mantle discontinuities (Morais 2012). The magnitude intervals of the teleseismic earthquakes, both PRFs and SRFs, were selected to be greater than $M_W \geq 5.5$ (Fig. 2). Approximately 1100 teleseismic earthquakes were processed through pre-data steps for each station, selected for their high-quality signals (high N/S), with approximately 500 events used to calculate the PRFs and around 260 events used for the SRFs. The locations of the events chosen for calculating PRFs and SRFs are displayed in Fig. 2. The data window for PRFs was selected as 160 seconds, with 50 seconds before and 110 seconds after the *P*-wave arrival. The data window for SRFs consisted of 100 seconds, with 90 seconds before and 10 seconds after the *S*-wave arrival. Preliminary data processing steps include linear trend, mean, taper, and removal of instrument response (Alkan, Çınar 2021; Alkan 2022a, b) using the Seismic Analysis Code software (Helffrich *et al.* 2013).

CALCULATING P- AND S-RECEIVER FUNCTIONS AND SIMULTANEOUS INVERSION

The receiver function method is a commonly used tool for detecting crustal and upper-mantle discontinuities beneath a seismic station by isolating the *P*-to-*S* and *S*-to-*P* converted waves (Vinnik *et al.* 2006; Silveira *et al.* 2010; Morais *et al.* 2015). This time series data is computed from three-component seismograms at teleseismic distances. The arrivals of these weakly converted waves from teleseismic events can be categorized into primary and secondary waves, which are reflected and refracted at seismic boundaries, such as the crust-mantle boundary and the lithosphere-asthenosphere boundary, as well as upper mantle discontinuities (410- and 660-km), close to the seismic station (Monna *et al.* 2019; Vinnik 2019). These waves exhibit very weak amplitudes, and it is necessary to enhance the signal-to-noise ratio. To achieve this, three important steps

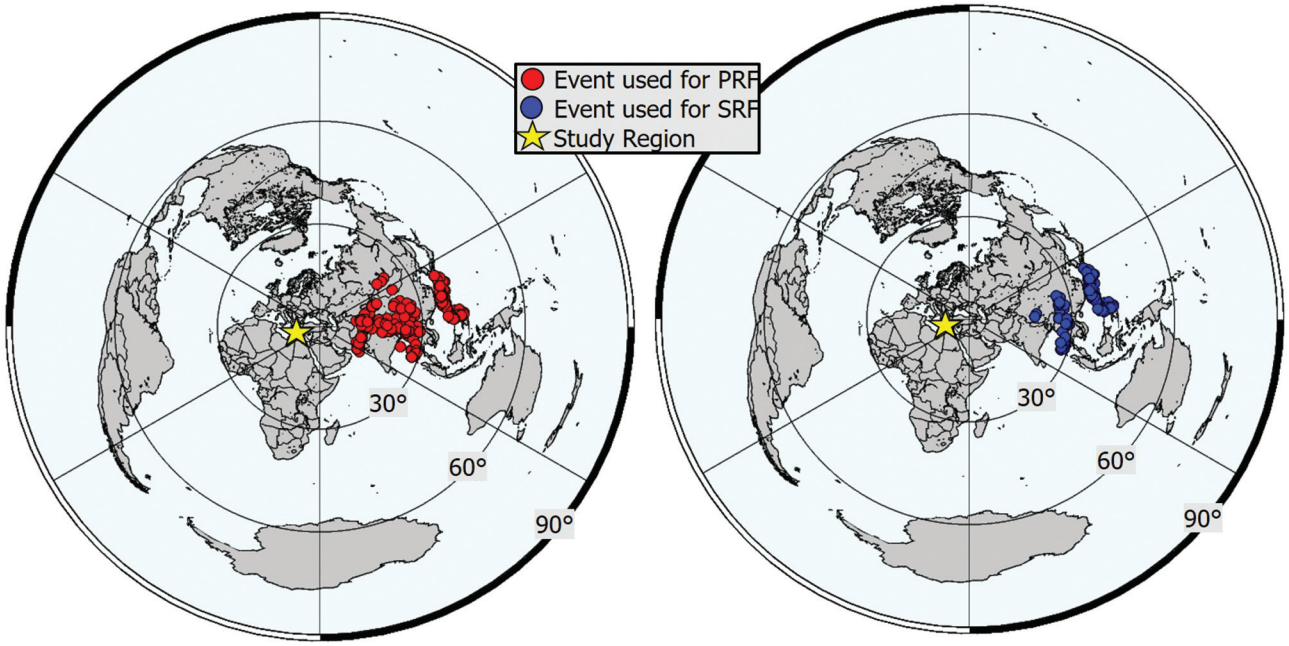

Fig. 2 Epicenter distribution of teleseismic earthquakes (red and blue circles) with magnitudes greater than $M_W \geq 5.5$ used to calculate PRFs (left) and SRFs (right). The study region is shown by the yellow star

Table 1 List of short-period, long-period, and broadband stations in the study region. Station information was taken from ORFEUS (https://orfeus-eu.org/stationbook/)

Network	Station Code	Starting Time	Latitude (Degree)	Longitude (Degree)	Elevation (m)	Streams by Code	Sensor Model
GE	KTHA	2013/06/19	36.256	23.062	360	LH	STS-2
GE	IMMV	2010/07/14	35.460	23.981	230	SH	STS-2
GE	ZKR	2003/09/16	35.114	26.216	254	SH	STS-2
GE	KARP	2009/11/25	35.547	27.161	524	LH	STS-2
HL	ARG	2003/10/20	36.213	28.121	148	SH	DR24
KO	YER	2012/05/24	37.136	28.285	729	BH	DM24
GE	APE	2008/04/29	37.072	25.523	608	SH	STS-2
HL	ITM	2003/10/20	37.178	21.925	423	SH	DR24

are employed: rotation, deconvolution, and stacking processes.

PRFs are computed by rotating into the *LQT* coordinate system. This rotation depends on the theoretical angle of incidence and ensures maximum energy of the *SV* wave on the *Q* component. In this rotation, the *P*-wave is primarily polarized along the *L* component, while the converted *Ps* phase is mainly observed on the *Q* component (Vinnik 1977). According to the time domain spiking deconvolution approach by Berkhout (1977), the *Q* component is deconvolved using the *L* component, referred to as the standard spike in the time domain. This deconvolution method is used to remove source complexities and mantle path effects (Dündar *et al*. 2016). After the deconvolution process, the *Q* component is termed the PRF. The deconvolved *Q* components are stacked with move-out time corrections using an adopted ray parameter of 6.4 s/°, corresponding to an epicentral distance of 67° (Kind, Vinnik 1988; Oreshin *et al.* 2008; Alkan *et al.* 2020). Stacking enhances the amplitudes of converted and multiple phases. The corrections are calculated for various trial conversion depths ranging from 0 to 800 km (Oreshin *et al.* 2011; Alkan *et al.* 2019). To constrain the velocity distribution for the major mantle discontinuities and minimize non-uniqueness, the absolute travel time residuals of *P* and *S* phases related to the *P410s* (44.0 s) and *P660s* (67.9 s) converted phases are useful, following Kennett and Engdahl (1991), Chevrot *et al.* (1999), and Kiselev *et al.* (2008). The travel time residuals are used to constrain the joint inversion of receiver functions within a depth range of less than 300 km (Grand 2002). *P*- and *S*-residuals are generated using the *P410s*-converted phase, assuming the difference between the absolute teleseismic *S* and *P* residuals (Vinnik *et al.* 1999; Oreshin *et al.* 2008).

SRFs are complementary to PRF for studying the mantle lithosphere and deeper due to the detection of converters from the Moho and upper mantle (Farra, Vinnik 2000; Huand *et al.* 2022; Monna *et al.* 2022). The calculation of SRF involves seismogram decomposition into the LAB coordinate system. In this axial rotation, the *L* component corresponds to the direction of the movement of the incident wave, and the *A* component to the direction of polarization of the principal *S* particle motion component in the plane, and the *L* component is deconvolved by the A component (spike pulse) (Vinnik 2019; Goev 2024). Before deconvolution, data are filtered using a Butterworth high-pass and low-pass filter. During the deconvolution step, the same method (Berkhout 1977) as in PRF is used in SRF. After the deconvolution process, the *L* component is termed the SRF. To isolate the *Sp* conversion and multiple reflected conversion phases generated by *SV*, the SRFs are stacked by applying weights that depend on the level of noise (Farra, Vinnik 2000; Monna *et al.* 2022). To account for the difference in slowness values changed between 0 to 0.2 s/°, the slant stacking (time correction) is calculated for several trial differential slownesses (difference between the epicentral distance of the seismic event and the average epicentral distance of the group of events) (Morais *et al.* 2015).

The *S*-wave velocity structures of crust and upper mantle discontinuities can be derived using the simultaneous inversion of PRFs and SRFs with teleseismic *P*-and *S*- travel time residuals. A basic assumption in the method is a homogeneous and isotropic Earth structure near the station, described by Vinnik *et al.* (2004, 2006). This algorithm is like the simulated annealing approach (Mosegaard, Vestergaard 1991). The synthetic receiver functions are generated using the Thomson-Haskell technique (Haskell 1962), associated with the Earth flattening transformation (Biswas 1972). In the performing inversion, the depth stacking trace of PRFs in the 0 km (shown in Figs 3 and 4) and the slant stacking trace of SRFs in 0 s/° (shown in Figs 5 and 6) are used. As the initial model, the *IASP91* standard velocity model (Kennett, Engdahl 1991) is applied at a depth of 300 km with 9 layers, which include *P*- and *S*-velocities, density calculated from Birch's law (Berteussen 1977), and the thickness of each layer. The misfit functions (*Ep(m)* for stacked PRFs and *Es(m)* for stacked SRFs), which are the *RMS* difference between the observed and synthetic functions (Vinnik *et al.* 2004; 2009), are minimized according to the rule of Metropolis (Metropolis *et al.* 1953) in cascade (Mosegaard, Tarantola 1995). For 4 random starting points, 100,000 models are tested to obtain a small misfit (Alkan *et al.* 2020), but for visualization, 10,000 models are kept shown in Figs 7 and 8.

RECEIVER FUNCTIONS STACKING

The arrival times of converted *Ps* phases from the Moho, 410 km, and 660 km boundaries can be obtained from PRF stacking. Using the *IASP91* Earth model (Kennett, Engdahl 1991), Chevrot *et al.* (1999) defined the arrival times of *Pmohos*, *P410s*, and *P660s* as 4.0 s, 44.0 s, and 67.9 s, respectively. Also, one phase labelled *Pslabs* is marked in the depth stacks of PRFs. According to observations of Li *et al.* (2003), this phase is interpreted as the subducting African lithosphere. Based on this criterion, the depth-stacking results of PRFs are calculated and presented for all stations in Table 2. For all stations, individual PRFs are changed from 35 to 91, and the distances range from 60° to 70°, with an average of 65.5°. As given in Table 2, a total of 452 teleseismic earthquakes are used for depth-stacking. The arriv-

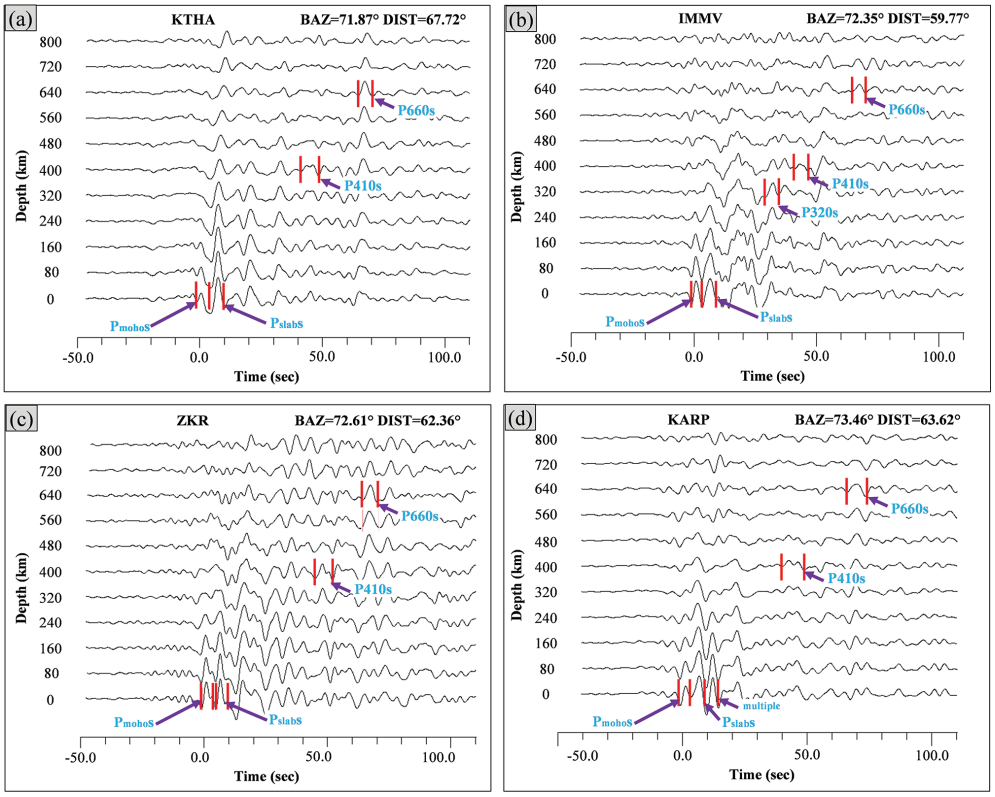

Fig. 3 Depth stacks with moveout of PRFs for stations **(a)** KTHA, **(b)** IMMV, **(c)** ZKR, and **(d)** KARP. Detailed information on each stacking is given in Table 2. Each trace corresponds to the trial depth in km attached to the left-hand side. The arrivals of *Ps* converted phases from Moho, Slab, 320-km, 410-km, and 660-km discontinuities are labelled *Pmohos, Pslabs*, *P320s*, *P410s*, and *P660s*

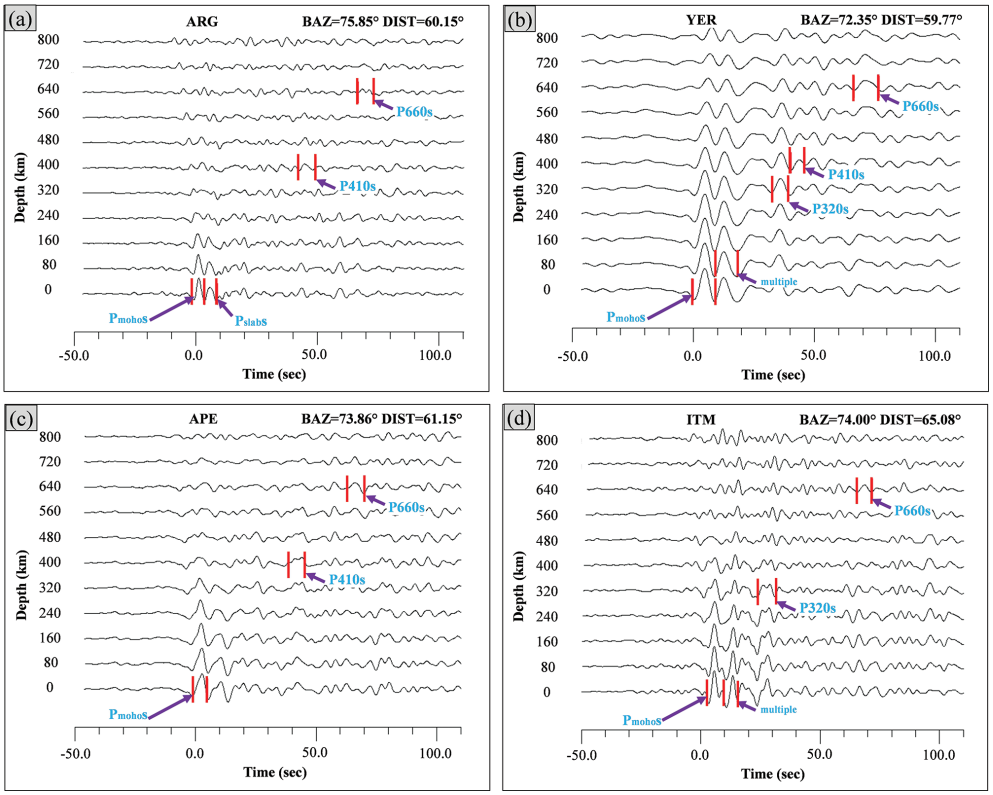

Fig. 4 Depth stacks with moveout of PRFs for stations **(a)** ARG, **(b)** YER, **(c)** APE, and **(d)** ITM. Detailed information on each stacking is given in Table 2. Each trace corresponds to the trial depth in km attached to the left-hand side. The arrivals of *Ps* converted phases from Moho, Slab, 320-km, 410-km, and 660-km discontinuities are labelled *Pmohos, Pslabs*, *P320s*, *P410s*, and *P660s*

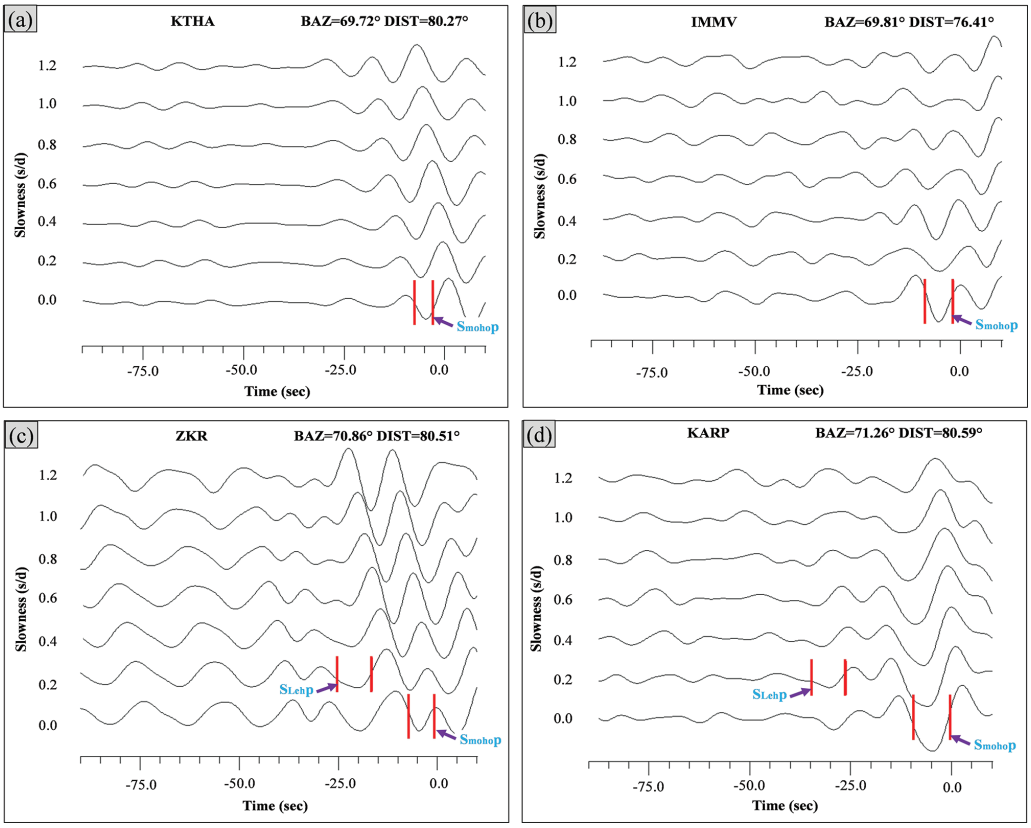

Fig. 5 Stacked SRFs for stations **(a)** KTHA, **(b)** IMMV, **(c)** ZKR, and **(d)** KARP. Detailed information on each stacking is given in Table 3. Each trace corresponds to the differential slowness in s/deg attached to the trace. The arrivals of *Sp* phases from the Moho and Lehmann discontinuities are labelled *Smohop* and *SLehp*

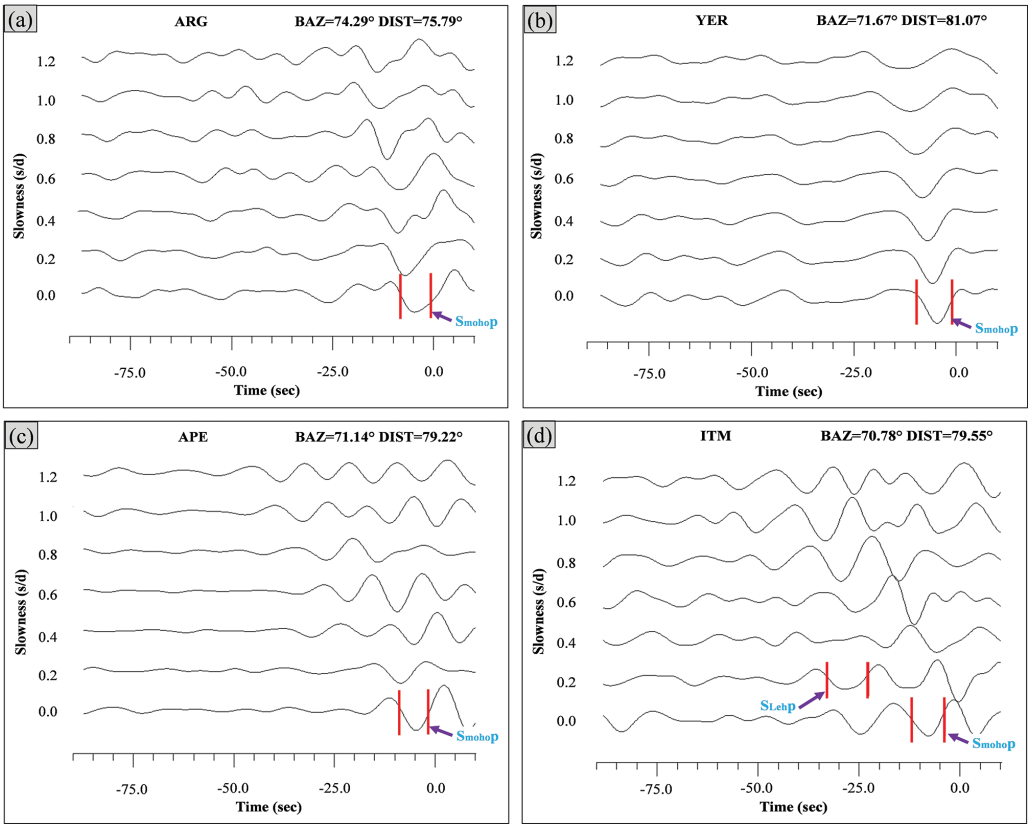

Fig. 6 Stacked SRFs for stations **(a)** ARG, **(b)** YER, **(c)** APE, and **(d)** ITM. Detailed information on each stacking is given in Table 3. Each trace corresponds to the differential slowness in s/deg attached to the trace. The arrival of *Sp* phases from the Moho discontinuity is labelled *Smohop*

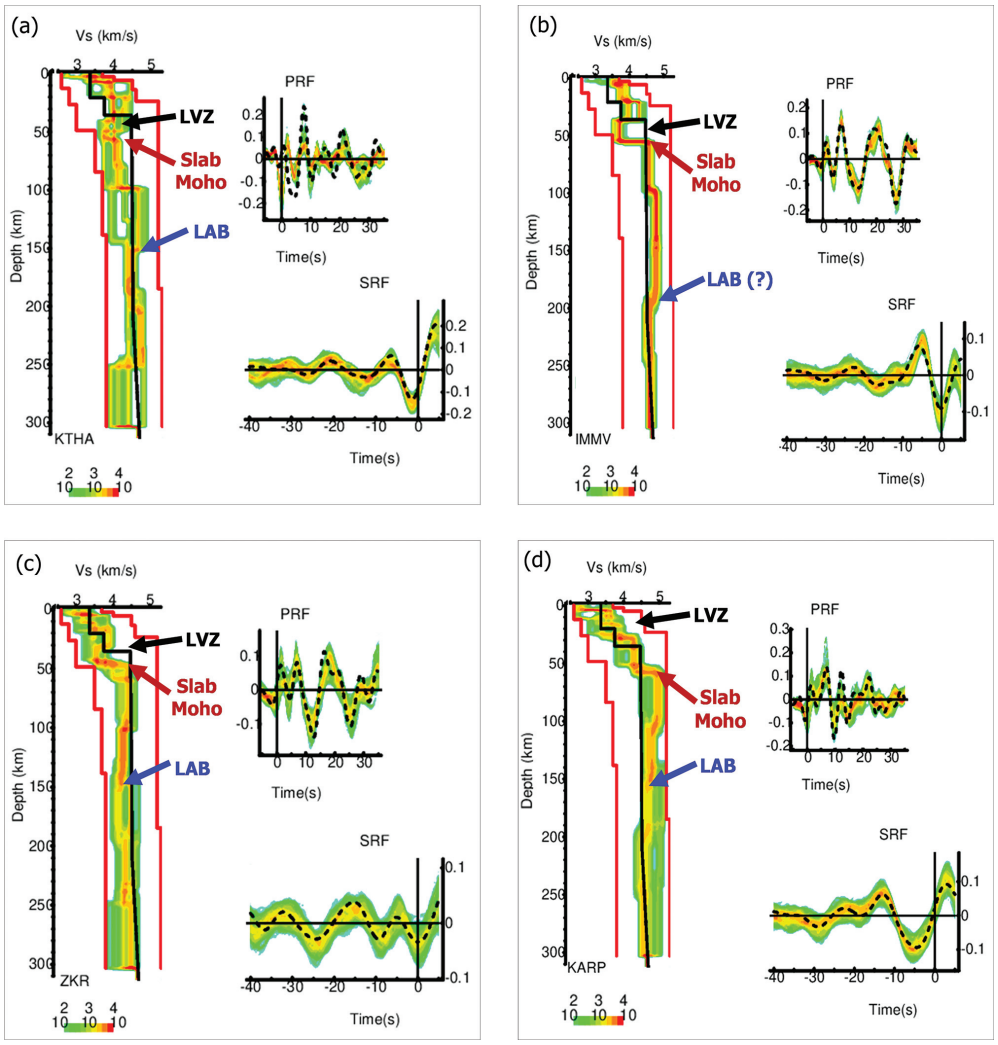

Fig. 7 Simultaneous inversion of PRFs and SRFs for stations **(a)** KTHA, **(b)** IMMV, **(c)** ZKR, and **(d)** KARP with teleseismic travel-time residuals, given in Table 2. Histograms of *Vs* are shown by color code. Black lines are the *IASP91* models (Kennett, Engdahl 1991). The limits of the search are shown by red lines. Black, claret red, and blue arrows represent the boundary of the low-velocity zone, Moho, and the lithosphere-asthenosphere boundaries, respectively. Histograms of the synthetic PRFs and SRFs are shown by the same colour code as the models; dashed lines are for the actual PRF and SRF

als of *Pmohos*, *P410s*, and *P660s* are figured out at all stations except the ITM station. Also, travel-time residuals of teleseismic *P*- and *S*-waves are calculated and used to constrain simultaneous inversion.

The stacking results of the PRFs for the stations show clear arrivals of *Pmohos*, *Pslabs*, multiple or crustal reflections, *P320s*, *P410s*, and *P660s* at the correct trial depths (Figs 3 and 4). Two distinct phase arrivals with high amplitude are observed between 0 and 10 seconds. These phases are marked as *Moho* and *Slab* (Figs 3 and 4), considering the continental crust and the present-day African Slab. *Ps* arrivals from the *Moho* discontinuity are noted in the time interval of 0.6 to 1.2 seconds at stations closer to the Hellenic trench, while the stacking results of YER, APE, and ITM located north of the subduction zone show arrival times of 4.7, 2.8, and 5.7 seconds, respectively (Figs 4b, 4c, and 4d). The second high-amplitude phase, labelled P*slabs*, appears between 5.8 and 7.4 seconds for southern stations (please see Table 2). Additionally, a positive polarity upper mantle phase, *P320s*, is observed in the stacking of IMMV, YER, and ITM at 32.3, 36.1, and 28.9 seconds, respectively (Figs 3b, 4b, and 4d). The *P320s* phase is still under discussion and is linked to a 320-km discontinuity in mid-upper mantle depths (250–350 km), which includes chemical heterogeneity related to the phase transition (Morais 2012). The *P410s* and *P660s* phases reduce the non-uniqueness of the joint inversion. The *P410s* phase is missed for detection in the depth-stacking of ITM. The travel times of the *P410s* phase for the stations ZKR, KTHA, ARG, and APE, detailed in Table 2, are delayed by 2–3 seconds, which can be attributed to a depression of the 410-km discontinuity. Conversely, for stations KARP, IMMV, and YER, the 410-km phase from the top of the tran-

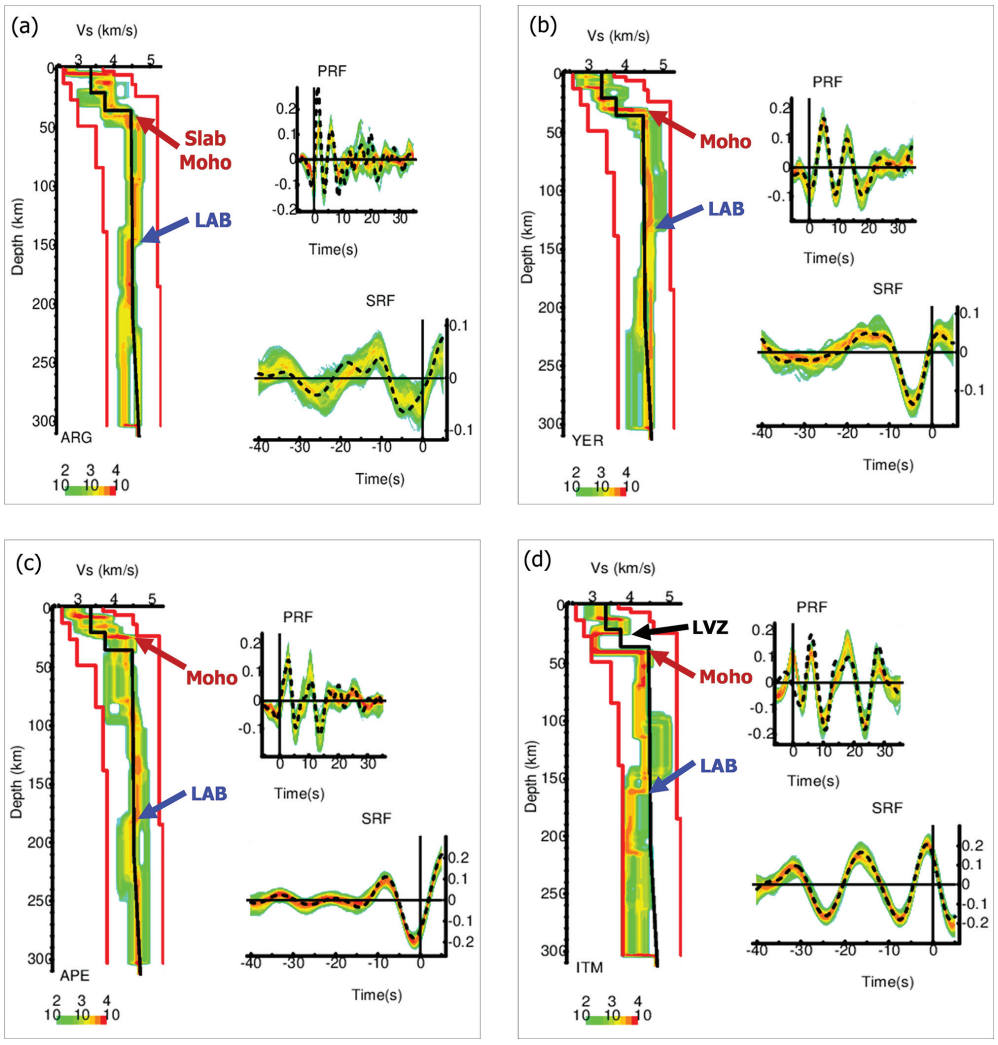

Fig. 8 Simultaneous inversion of PRFs and SRFs for stations **(a)** ARG, **(b)** YER, and **(c)** APE with teleseismic travel-time residuals and **(d)** ITM without teleseismic travel-time residuals, given in Table 2. Histograms of *Vs* are shown by colour code. Black lines are the *IASP91* models (Kennett, Engdahl 1991). The limits of the search are shown by red lines. Black, claret red, and blue arrows stand for the boundary of the Low-velocity zone, Moho, and the lithosphere-asthenosphere boundaries, respectively. Histograms of the synthetic PRFs and SRFs are shown by the same colour code as the models; dashed lines are for the actual PRF and SRF

sition zone arrives earlier (approximately 2 seconds) as shown in Table 2, indicating high *S*-wave velocities around 300 km, an uplift around 410 km, and a high-velocity upper mantle in the southern Aegean (Li *et al.* 2003). The travel time arrivals of the *P660s* phases are observed in all depth stacking, where some of these arrivals are earlier (ZKR, KTHA, IMMV, and APE) and others are later arrivals (KARP, ITM, YER, and ARG). It is relative to the *IASP91* standard earth model. The late arrival times of the *P660*s at the stations (shown in Table 2) suggest that the 660-km discontinuity is depressed by several kilometres and may be linked to the subducted slab beneath it. Additionally, Li *et al*. (2003) noted that the 410-km discontinuity is roughly 10 km thicker than predicted by the *IASP91* model, which is associated with an approximate temperature reduction of ~ 80°.

The slowness-stacking parameters of SRFs are presented in Table 3 for all stations. Additionally, the stacking results of SRFs are illustrated in Figs 5 and 6. The number of individual SRFs with an average epicentral distance of 80° ranges between 19 and 40 for each station. As given in Table 3, a total of 237 teleseismic earthquakes are used for slowness-stacking. Figures 5 and 6 display the largest amplitudes from the crustal phase (*Smohop*) at 0.0 s/°. The standard noise errors (*rms* value of noise in the stacking) for all slowness-stacking vary between 0.008 and 0.035. These values are compared to the amplitude value of the *Smohop* phase, and nearly four times the *rms* amplitude of noise is expected for successful stacking results (Morais 2012). *Sp* phases from the Moho, with negative polarity corresponding to positive discontinuities, are detected around –4.6 s at 0.0 s/° differential slowness for all results, except for station ITM, which is observed at –7.9 s at 0.0 s/°. Furthermore, a

Table 2 Parameters of all PRFs stacking for each station. 'Baz' and 'DIST' are the average back azimuth and epicentral distances. *Pmohos*, *Pslabs*, *P410s*, and *P660s* correspond to the arrival times of *Ps* phases. *dTp* and *dTs* are travel-time residuals of teleseismic P and S waves

Station	BAZ (deg)	DIST (deg)	Number of records	P*mohos* (s)	P*slabs* (s)	P410s (s)	P660s (s)	dTp (s)	dTs (s)
KTHA (LH)	71.87	67.72	55	0.6	7.4	46.11	67.25	0.5	1.5
IMMV (SH)	72.35	59.77	70	1.0	6.6	43.13	67.50	-0.45	-1.35
ZKR (SH)	72.61	62.36	91	0.9	6.6	47.90	67.47	1.0	3.0
KARP (LH)	73.46	63.62	53	1.2	6.7	42.60	69.94	-0.6	-1.8
ARG (SH)	75.85	60.15	56	1.2	5.8	44.53	68.42	0.25	0.75
YER (BB)	73.67	70.19	44	4.7	–	43.75	70.94	-0.1	-0.3
APE (SH)	73.86	61.15	48	2.8	–	44.11	66.07	0.1	0.3
ITM (SH)	74.00	65.08	35	5.7	–	–	68.64	–	–

Table 3 Parameters of all SRFs stacking for each station. 'BAZ' and 'DIST' are the average back azimuth and epicentral distances. *Smohop* and *SLehp* are the arrival times of Moho and the Lehmann discontinuity, respectively. Noise is the *RMS* value (σ) of the *Smp* phase, respectively

Station	BAZ (deg)	DIST (deg)	Number of records	S*mohop* (s)	S*Lehp* (s)	Amplitude of S*mohop*	Noise (σ)
KTHA (LH)	69.72	80.27	35	–4.6	–	0.13	0.011
IMMV (SH)	69.81	76.41	34	–5.4	–	0.09	0.010
ZKR (SH)	70.86	80.51	40	–4.6	–20.2	0.02	0.008
KARP (LH)	71.26	80.59	28	–4.8	–28.5	0.09	0.010
ARG (SH)	74.29	75.79	27	–4.6	–	0.06	0.009
YER (BB)	71.67	81.07	32	–4.6	–	0.13	0.011
APE (SH)	71.14	79.22	19	–4.6	–	0.18	0.015
ITM (SH)	70.78	79.55	22	–7.9	–28.6	0.18	0.035

phase *Sp* from the Lehmann discontinuity with negative polarity, labelled *Slehp*, is noted in the stacking results of ZKR, KARP, and ITM at a slowness of 0.2 s/°. The arrival times of these phases are –20.2 s, –28.5 s, and –28.6 s, respectively (Fig. 5c, 5d, and 6d). The phase *Slehp*, with negative polarity, is associated with a depth between 200 km and 250 km, corresponding to the base of the low *S*-velocity layer (Vinnik *et al.* 2004).

RESULTS OF SIMULTANEOUS INVERSION AND DISCUSSION

The *S*-wave velocity histograms for eight stations obtained from the simultaneous inversion of PRFs and SRFs are illustrated in Figs 7 and 8. *S*-wave velocity models are interpreted with the stacking results presented in Figs 3 to 6. *S*-wave velocity results from the southern stations, KTHA, IMMV, ZKR, KARP, and ARG, are evaluated as the first group, closer to the Hellenic subduction zone. However, the velocity results from the northern stations, YER, APE, and ITM, are analyzed in the second group behind the Hellenic trench to the north. Overall, the *S*-wave velocity models for KTHA, IMMV, ZKR, KARP, and ARG stations exhibit similar characteristics. On the other hand, the stations YER, APE, and ITM are consistent with one another and earlier studies in the literature. Also, the depths of lithospheric discontinuities calculated from the simultaneous inversion are summarized in Table 4.

The first sharp increases in *S*-wave velocities are observed at depths of 45 km to 56 km for stations KTHA, IMMV, ZKR, KARP, and ARG, as indicated by claret red arrows in Figs 7 and 8. At station KTHA (Fig. 7a), the *S*-wave velocity change at a depth of 51 km ranges from 3.8 to 4.1 km/s. At station IMMV (Fig. 7b), the *S*-wave velocity at a depth of 53 km increases from 3.7 to 4.6 km/s. At station ZKR (Fig. 7c), the *S*-wave velocity at a depth of 48 km varies from 3.7 to 4.4 km/s. At station KARP (Fig. 7d), the *S*-wave velocity jump occurs at a depth of 56 km, changing between 4.1 and 4.8 km/s. At station ARG (Fig. 8a), the *S*-wave velocity increases between 4.0 and 4.6 km/s at a depth of 45 km. In terms of the geological locations of the stations, these depth values are quite significant for the continental Aegean Moho. These high depths correspond to the subducted African lithosphere. Previous crustal studies (Li *et al.* 2003; van der Meijde *et al.* 2003; Sodoudi *et al.* 2006, 2015; Zhu *et al.* 2006; Di Luccio, Pasyanos 2007; Sachpazi *et al.* 2016; Dogru *et al.* 2018; Karabulut *et al.* 2019) found the Moho depths of the Aegean and western Anatolia to be located 25 to 30 km beneath Kythira, Crete, Karpathos, and Rhodes, near the north of the Hellenic Trench. However, Li *et al.* (2003) observed that converted *Ps* phases from the oceanic Moho of the subducted African Plate are detected around Crete Island at depths of 51 to 69 km. Similar

Table 4 Depths of Moho, Slab Moho, low-velocity zone (LVZ), and LAB calculated from the simultaneous inversion of PRFs and SRFs

Station Code	Moho (km)	Slab Moho (km)	LVZ (km)	LAB (km)
KTHA (LH)	–	51	41	148
IMMV (SH)	–	53	35	191
ZKR (SH)	–	48	33	144
KARP (LH)	–	56	30	150
ARG (SH)	–	45	-	142
YER (BB)	29	-	-	130
APE (SH)	24	-	-	179
ITM (SH)	40	-	23	157

to the findings of Li *et al.* (2003), two *Ps* converted phases, labelled *Pmohos* and *Pslabs*, are identified in the depth-stacking presented in Figs 3 and 4. The converted Moho phase appears weak in the deeper regions of the African Plate near the subduction zone. One of these phases is associated with the Aegean Moho, while the other corresponds to the oceanic Moho of the descending African Plate. Therefore, a thicker Moho than the Aegean continental type is calculated in the *S*-wave velocity models derived from simultaneous inversion (Figs 7 and 8). S-wave velocities in this study also closely match the findings of Endrun *et al*. (2011) regarding the anisotropic fabric in the lower crust, which trends parallel to the Miocene extension direction, illustrating distributed viscous flow in the lower crust and lithospheric mantle around the Cyclades. Also, Erbek-Kiran *et al.* (2025) defined the high gravity values around the Cretan Sea, signifying the dipping African Slab.

The Moho depths beneath YER, APE, and ITM stations, as listed in Table 4, located in the northern part of the study region, are associated with the continental crust related to western Anatolia, the Aegean Sea, and western Greece. The *S*-wave velocity changes in the crust-mantle transition at a depth of 29 km from 3.5 km/s to 4.3 km/s beneath station YER (Fig. 8b). Kind *et al.* (2015) highlighted the crustal and lithospheric discontinuities beneath the Aegean and Anatolian regions based on the *S*-receiver function technique. They determined the crustal thickness to be around 25 km beneath western Anatolia. The Moho thickness and *S*-wave velocities beneath station YER align with the findings of Kind *et al.* (2015) and other receiver function studies (Tezel *et al.* 2013; Vanacore *et al.* 2013). The Moho discontinuity is measured at 24 km beneath station APE, with velocities increasing to 3.7 km/s in the crust and 4.3 km/s in the upper mantle (Fig. 8c). Beneath APE, this depth has been commented as clearly normal Moho and agrees with Li *et al.* (2003) and Zhu *et al.* (2006). The Moho discontinuity is found at 40 km beneath the ITM station located on the Peloponnesus, with *S*-wave velocities ranging from 3.0 km/s in the crust to 4.3 km/s in the upper mantle (Fig. 8d). Using the surface wave tomography algorithm, Karagianni *et al.* (2005) observed a crustal thickness of 42 ± 2 km in western Greece along the Hellenides mountain range, and also calculated approximately 22 km of Moho depth beneath the central Aegean basin. Sodoudi *et al.* (2015) observed the thickest crust at ~ 48 km beneath the Peloponnesus, while a thinner crust of 23 to 28 km was observed beneath the central Aegean Sea and western Türkiye. Additionally, Sachpazi *et al.* (2016) imaged crustal and upper-mantle structures beneath the western Hellenic subduction zone through receiver function analysis. They obtained the first clear positive receiver function amplitudes at a depth of about 30 km associated with the Aegean Moho. However, the second positive amplitude corresponded to the Moho of the subducting plate, starting at a depth of 40–50 km beneath the Peloponnesus (Fig. 8d). Based on the satellite marine gravity data, Tirel *et al.* (2004) identified the three different crustal types as Aegean, Cyclades, and Crean Sea with a mean Moho depth of ~ 25 km. They also found a crustal thinning zone of coverage in the north of the Hellenic Trench, controlled by the back-arc extension and the active slab mechanism. Sachpazi *et al.* (2025) calculated the Aegean plate's Moho in southern-central Peloponnesus at ~ 35 km depth. On the other hand, *S*-wave velocity histograms show that the low-velocity zone, as indicated by black arrows in Figs 7 and 8, have been observed in the crustal depths beneath the stations KTHA, IMMV, ZKR, KARP, and ITM. These low-velocity zones may be correlated to weakening crustal intrusions, fully serpentinized peridotites, and low-velocity mantle accretionary wedge above the subducted slab (Mueller 1977; Bohnhoff *et al.* 2001; Li *et al.* 2003; Karagianni *et al.* 2005).

The *S*-wave velocity trends in the histograms can be interpreted to determine possible LAB depths. LAB is approximately 155 km for the first group (KTHA, IMMV, ZKR, KARP, and ARG), as indicated by the blue arrows shown in Figs 7, 8, and Table 4. *S*-wave trends decrease after this approximate depth. Upon a detailed examination of the velocity histograms, an *S*-wave velocity of 4.4 km/s can be seen for the KTHA at a depth of 148 km (Fig. 7a). The LAB depth at the IMMV station is observed to be around 191 km with Vs = 4.6 km/s, while a reduction in *S*-wave velocity is noted at a depth of 144 km, decreasing from 4.3 km/s to 4.2 km/s beneath station ZKR. The LAB thickness beneath IMMV is anomalously large compared to other stations. According to the *S*-wave histograms for the KARP (Fig. 7d) and ARG (Fig. 8a) stations, the LAB is indicated at 150 km (Vs = 4.7 km/s) and 142 km (Vs = 4.4 km/s), respectively. Sodoudi *et al.* (2006) estimated similar results beneath mainland Greece of Aegean LAB

depth. The tomography models of Biryol *et al.* (2011) showed the most significant fast anomalies located on the Hellenic and Cyprus trenches extended down to the depths of 300 km, interpreted as the segments of the subducting African oceanic lithosphere. Gönenç and Akgün (2012) discovered that the deep structures (130 and 170 km) passed through the north of the Cretan Sea region using gravity data. This region was described as the terminus of the African Oceanic mantle lithosphere. The deep and intermediate-depth events mainly clustered below the Hellenic Arc (depth ~ 180 km), associated with the continuity oceanic slab (Faccenna *et al.* 2014). Also, the present high velocity anomalies beneath the Aegean Sea may indicate the physical model of slab sinking in a viscously stratified mantle. Based on gravity models, Dogru *et al.* (2018) calculated the LAB depth to be around 140 km beneath the southern Aegean Sea, and this depth was associated with the dynamic subduction zone in the Hellenic Arc. The lithosphere beneath the Mediterranean was believed to be Oceanic lithosphere, with earthquakes reaching 150 km (McKenzie 2020). Toyokuni and Zhao (2025) observed the low-velocity zones in the crust and shallow mantle in the Aegean Sea, while the high-velocity images associated with the subducted slabs (150–450 km depths) were visible beneath the Hellenic and Cyprus Trenches, which may reflect a vertical slab subduction. Therefore, the depth values of LABs obtained beneath the stations are associated with the African Slab.

In the inversion models of the stations YER, APE, and ITM, the LAB appears strongly at 130, 179, and 157 km in the direction from east to west. The *S*-wave velocities at these boundaries decrease from 4.6 to 4.5 km/s, 4.6 to 4.4 km/s, and from 4.5 to 4.0 km/s, respectively. The LAB depth beneath station YER corresponds to the lithosphere of the Anatolian Plate, not related to the subduction of the African Slab. In SRF stacking of Kind *et al.* (2015), the LAB reached down to almost 150 km depth beneath western Anatolia and the central Aegean Sea. Also, Sodoudi *et al.* (2006) reported that the dip of the subducting African Plate was shallower beneath the Peloponnesus and flattened out beneath the central Aegean. The Aegean lithosphere was calculated as having a similar depth around station ITM. Salaün *et al.* (2012) showed that the Hellenic Slab was identified as a continuous high-velocity zone along with Crete, Santorini, and Mykonos. The slab thickness was approximately 150 km. Therefore, LAB depths for the first and second groups are found close to each other in the Aegean Sea.

CONCLUSIONS

In this study, one-dimensional *S*-wave velocity models to a depth of 300 km beneath the Aegean region are estimated using the simultaneous inversion of PRFs and SRFs with teleseismic travel-time residuals. For the joint inversion, high-quality teleseismic data recorded at short, long, and broadband seismic stations are used. The main findings of this study are given as follows:

(1) The Moho discontinuities beneath stations KTHA, IMMV, ZKR, KARP, and ARG are the phases from the oceanic Moho of the subducted African Plate, while the crust-mantle transition under stations YER, APE, and ITM is continental crust related to western Anatolia, the Aegean Sea, and western Greece, which agrees with the previous receiver function studies.

(2) In the depth stacking results of the southern stations, both the continental crust and the African Slab appear. In addition, the *P410s* and *P660s* phases are also obviously observed in stacking, constraining simultaneous inversion. On the other hand, in the slowness stacking of ZKR, KARP, and ITM, the phase *Slehp* is detected, associated with a low *S*-velocity layer at a depth between 200 km and 250 km.

(3) Seismic stations operated throughout the Peloponnesus, Kythira, Crete, Karpathos, and Rhodes display low *S*-wave velocity zones at lower crustal levels, which may be associated with weakening crustal intrusions and mantle accretionary wedge.

(4) The thickness of the lithosphere estimated from joint inversion of PRFs and SRFs varies from ~ 140 to ~ 150 km beneath the southern stations, related to the African Slab. However, an anomalous value prevails beneath the station IMMV, where inversion reveals the thickness of the lithosphere to be 190 km, which may reflect a vertical slab subduction of the Hellenic Arc.

ACKNOWLEDGMENTS

I thank the ORFEUS Data Center (https://www.orfeus-eu.org/data/eida/) for providing the teleseismic earthquake data. I would like to express my special thanks to Dr. Lev Vinnik (RIP), Dr. Sergey Oreshin, and Dr. Aydın Büyüksaraç for their scientific support. Finally, I thank the editor-in-chief and anonymous reviewers for their constructive and detailed reviews. Some figures were produced using Generic Mapping Tools software (Wessel *et al.* 2019). Receiver function processes are performed using the Seismic Handler software package (Stemmler, Walther 2013).

REFERENCES

Alkan, H. 2022a. Joint inversion of Rayleigh wave phase velocities and P-receiver functions along the East Anatolian fault zone. *Journal of Seismology 26*, 79–100. https://doi.org/10.1007/s10950-021-10065-6

Alkan, H. 2022b. Crustal structure in and around the East Anatolian volcanic belt by using receiver functions stacking. *Journal of African Earth Sciences 191*, 104532. https://doi.org/10.1016/j.jafrearsci.2022.104532

Alkan, H., Çınar, H. 2021. The lithospheric structure underneath the Circum Black Sea: Teleseismic receiver functions and Rayleigh wave phase velocity analysis. *Journal of Asian Earth Sciences 206*, 104652. https://doi.org/10.1016/j.jseaes.2020.104652

Alkan, H., Çınar, H., Oreshin, S., Vinnik, L. 2019. Investigation of the crustal and upper-mantle structure of the eastern Pontides orogenic belt (NE, Turkey): a receiver-function study. *Journal of Seismology 23*, 473–491. https://doi.org/10.1007/s10950-019-09818-1

Alkan, H., Çınar, H., Oreshin, S. 2020. Lake Van (Southeastern Turkey) Experiment: Receiver Function Analyses of Lithospheric Structure from Teleseismic Observations. *Pure and Applied Geophysics 177*, 3891–3909. https://doi.org/10.1007/s00024-020-02447-7

Alkan, H., Büyüksaraç, A., Bektaş, Ö., Işık, E. 2021. Coulomb stress change before and after 24. 01. 2020 Sivrice (Elazığ) earthquake (Mw = 6.8) on the East Anatolian Fault Zone. *Arabian Journal of Geosciences 14(23)*, 2648.

Berkhout, A.J. 1977. Least square inverse filtering and wavelet deconvolution. *Geophysics 42*, 1369–1383.

Berteussen, K.A. 1977. Moho depth determinations based on spectral ratio analysis of NORSAR long-period P waves. *Physics of the Earth and Planetary Interiors 15*, 13–27.

Biryol, C.B., Beck, S.L., Zandt, G., Özacar, A.A. 2011. Segmented African lithosphere beneath the Anatolian region inferred from teleseismic P-wave tomography. *Geophysical Journal International 184(3)*, 1037–1057. https://doi.org/10.1111/j.1365-246X.2010.04910.x

Biswas, N.N. 1972. Earth-flattening procedure for the propagation of Rayleigh wave. *Pure and Applied Geophysics 96*, 61–74.

Bohnhoff, M., Makris, J., Papanikolaou, D., Stavrakakis, G. 2001. Crustal investigation of the Hellenic subduction zone using wide aperture seismic data. *Tectonophysics 343*, 239. https://doi.org/10.1016/S0040-1951(01)00264-5

Bohnhoff, M., Rische, M., Meier, T., Becker, D., Stavrakakis, G., Harjes, H.P. 2006. Microseismic activity in the Hellenic Volcanic Arc, Greece, with emphasis on the seismotectonic setting of the Santorini–Amorgos zone. *Tectonophysics 423(1–4)*, 17–33. https://doi.org/10.1016/j.tecto.2006.03.024

Bozkurt, E. 2001. Neotectonics of Turkey – a synthesis. *Geodinamica Acta 14*, 3–30. https://doi.org/10.1016/S0985-3111(01)01066-X

Briole, P., Ganas, A., Elias, P., Dimitrov, D. 2021. The GPS velocity field of the Aegean. New observations, contribution of earthquakes, crustal blocks model. *Geophysical Journal International 226(1)*, 468–492. https://doi.org/10.1093/gji/ggab089

Chevrot, S., Vinnik, L., Montagner, J.P. 1999. Global scale analysis of the mantle Pds phases. *Journal of Geophysical Research 104*, 203–219. https://doi.org/10.1029/1999JB900087

Cossette, É.P., Audet, D., Schneider, Grasemann, B. 2016. Structure and anisotropy of the crust in the Cyclades, Greece, using receiver Functions constrained by in situ rock textural data. *Journal of Geophysical Research: Solid Earth 121*, 2661–2678. https://doi.org/10.1002/2015JB012460

Di Luccio, F., Pasyanos, M.E. 2007. Crustal and upper-mantle structure in the Eastern Mediterranean from the analysis of surface wave dispersion curves. *Geophysical Journal International 169(3)*, 1139–1152. https://doi.org/10.1111/j.1365-246X.2007.03332.x

Dimitriadis, I., Karagianni, E., Panagiotopoulos, D., Papazachos, C., Hatzidimitriou, P., Bohnhoff, M., Rische, M., Meier, T. 2009. Seismicity and active tectonics at Coloumbo Reef (Aegean Sea, Greece): Monitoring an active volcano at Santorini Volcanic Center using a temporary seismic network. *Tectonophysics 465(1–4)*, 136–149. https://doi.org/10.1016/j.tecto.2008.11.005

Dogru, F., Pamukcu, O., Gonenc, T., Yildiz, H. 2018. Lithospheric structure of western Anatolia and the Aegean Sea using GOCE-based gravity field models. *Bollettino di Geofisica Teorica ed Applicata 59(2)*, 135–160.

Drymoni, K., Browning, J. Gudmundsson, A. 2022. Spatial and temporal volcano tectonic evolution of Santorini volcano, Greece. *Bulletin of Volcanology 84*, 60. https://doi.org/10.1007/s00445-022-01566-4

Dündar, S., Dias, N.A., Silveira, G., Kind, R., Vinnik, L., Matias, L., Bianchi, M. 2016. Estimation of the Crustal Bulk Properties Beneath Mainland Portugal from P-Wave Teleseismic Receiver Functions. *Pure and Applied Geophysics 173*, 1949–1970. https://doi.org/10.1007/s00024-016-1257-4

Emre, Ö., Duman, T.Y., Özalp, S., Şaroğlu, F., Olgun, Ş., Elmacı, H., Çan, T. 2018. Active fault database of Turkey. *Bulletin of Earthquake Engineering 16(8)*, 3229–3275. https://doi.org/10.1007/s10518-016-0041-2

Endrun, B., Lebedev, S., Meier, T., Tirel, C., Friederich, W. 2011. Complex layered deformation within the Aegean crust and mantle revealed by seismic anisotropy. *Nature Geoscience 4(3)*, 203–207.

Erbek-Kiran, E., Ates, A. Dolmaz, M.N. 2025. Exploring the crustal structure of the Aegean Sea from satellite bouguer gravity, magnetic data, and seismological data. *Geo-Marine Letters 45*, 12. https://doi.org/10.1007/s00367-025-00800-0

Evangelidis, C.P. 2017. Seismic anisotropy in the Hellenic subduction zone: Effects of slab segmentation and subslab mantle flow. *Earth and Planetary Science Letters 480*, 97–106. https://doi.org/10.1016/j.epsl.2017.10.003

Faccenna, C., Becker, T.W., Auer, L., Billi, A., Boschi, L., Brun, J.P., Capitanio, F.A., Funiciello, F., Horvath, F., Jolivet, L., Piromallo, C., Royden, L., Rossetti, F., Serpelloni, E. 2014. Mantle dynamics in the

Mediterranean. *Reviews of Geophysics 52(3)*, 283–332. https://doi.org/10.1002/2013RG000444

Farra, V., Vinnik, L. 2000. Upper mantle stratification by P and S receiver functions. *Geophysical Journal International 141*, 699–712. https://doi.org/10.1046/j.1365-246x.2000.00118.x

Gönenç, T., Akgün, M. 2012. Structure of the Hellenic Subduction Zone from Gravity Gradient Functions and Seismology. *Pure and Applied Geophysics 169*, 1231–1255. https://doi.org/10.1007/s00024-011-0391-2

Grand, S.P. 2002. Mantle shear-wave tomography and the fate of subducted slabs. *Philosophical Transactions of the Royal Society of London. Series A: Mathematical, Physical and Engineering Sciences 360(1800)*, 2475–2491. https://doi.org/10.1098/rsta.2002.1077

Goev, A.G. 2024. Velocity structure of the Earth's crust and upper mantle in the Pechenga ore region and adjacent areas in the northwestern part of the Lapland-Kola orogen by the receiver function technique. *Записки Горного института 266*, 188–198. (In English).

Haskell, N.A. 1962. Crustal reflection of plane P and SV waves. *Journal of Geophysics Research 67*, 4751–4767.

Helffrich, G., Wookey, J., Bastow, I. 2013. *The Seismic Analysis Code, A Primer and User's Guide*. Cambridge United Kingdom. https://doi.org/10.1017/CBO9781139547260

Huang, S.H., Thybo, H., Dong, S.W., Artemieva, I.M., He, R.Z., Han, B.F., Zhou, Q., Shi, W. 2022. Upper mantle seismic structure in the Ordos Block, China. *Journal of Geodynamics 151*, 101921. https://doi.org/10.1016/j.jog.2022.101921

Karabulut, H., Paul, A., Özbakır, A.D., Ergün, T., Şentürk, S. 2019. A new crustal model of the Anatolia–Aegean domain: evidence for the dominant role of isostasy in the support of the Anatolian plateau. *Geophysical Journal International 218(1)*, 57–73. https://doi.org/10.1093/gji/ggz147

Karagianni, E.E., Papazachos, C.B., Panagiotopoulos, D.G., Suhadolc, P., Vuan, A., Panza, G.F. 2005. Shear velocity structure in the Aegean area obtained by inversion of Rayleigh waves. *Geophysical Journal International 160(1)*, 127–143. https://doi.org/10.1111/j.1365-246X.2005.02354.x

Kassaras, I., Kapetanidis, V., Karakonstantis, A., Papadimitriou, P. 2020. Deep structure of the Hellenic lithosphere from teleseismic Rayleigh-wave tomography. *Geophysical Journal International 221(1)*, 205–230. https://doi.org/10.1093/gji/ggz579

Kennett, B.L.N., Engdahl, E.R. 1991. Travel times for global earthquake location and phase identification. *Geophysical Journal International 105*, 429–465.

Kind, R., Vinnik, L.P. 1988. The upper-mantle discontinuities underneath the GRF array from P-to-S converted phases. *Journal of Geophysics 62*, 138–147. https://n2t.net/ark:/88439/y067070

Kind, R., Tilmann, F., Sodoudi, F., Taymaz, T., Bulut, F., Yuab, X., Can, B., Schneider, F. 2015. Thickness of the lithosphere beneath Turkey and surroundings from S-receiver functions. *Solid Earth 6*, 971–984. https://doi.org/10.5194/se-6-971-2015

Kiselev, S., Vinnik, L., Oreshin, S., Gupta, S., Rai, S.S., Singh, A., Kumar, M.R., Mohan, G. 2008. Lithosphere of the Dharwar craton by joint inversion of P and S receiver functions. *Geophysical Journal International 173*, 1106–1118. https://doi.org/10.1111/j.1365-246X.2008.03777.x

Kosarev, G.L., Oreshin, S.I., Vinnik, L.P., Kiselev, S.G., Dattatrayam, R.S., Suresh, G., Baidya, P.R. 2013. Heterogeneous lithosphere and the underlying mantle of the Indian sub-continent. *Tectonophysics 592*, 175–186. https://doi.org/10.1016/j.tecto.2013.02.023

Li, X., Bock, G., Vafidis, A., Kind, R., Harjes, H.P., Hanka, W., Wylegalla, K., van der Meijde, M., Yuan, X. 2003. Receiver function study of the Hellenic subduction zone: imaging crustal thickness variations and the oceanic Moho of the descending African lithosphere. *Geophysical Journal International 155(2)*, 733–748. https://doi.org/10.1046/j.1365-246X.2003.02100.x

Makris, J., Papoulia, J., Papanikolaou, D., Fasoulaka, C. 2022. Crustal structure beneath the Cyclades Metamorphic Core Complex, Aegean Sea, Greece. *Tectonophysics 842*, 229–585. https://doi.org/10.1016/j.tecto.2022.229585

McClusky, S., Balassanian, S., Barka, A., Demir, C., Ergintav, S., Georgiev, I., Gurkan, O., Hamburger, M., Hurst, K., Kahle, H., Kastens, K., Kekelidze, G., King, R., Kotzev, V., Lenk, O., Mahmoud, S., Mishin, A., Nadariya, M., Ouzounis, A., Paradissis, D., Peter, Y., Prilepin, M., Reilinger, R., Sanli, I., Seeger, H., Tealeb, A., Toksöz, M.N., Veis, G. 2000. Global positioning system constraints on plate kinematics and dynamics in the eastern Mediterranean and Caucasus. *Journal of Geophysical Research 105*, 5695–5719. https://doi.org/10.1029/1999JB900351

McKenzie, D. 1972. Active Tectonics of the Mediterranean region. *Geophysical Journal International 30(2)*, 109–185.

McKenzie, D. 2020. The structure of the lithosphere and upper mantle beneath the Eastern Mediterranean and Middle East. *Mediterranean Geoscience Reviews 2*, 311–326. https://doi.org/10.1007/s42990-020-00038-1

Meier, T., Rische, M., Endrun, B., Vafidis, A., Harjes, H.P. 2004. Seismicity of the Hellenic subduction zone in the area of western and central Crete observed by temporary local seismic networks. *Tectonophysics 383(3–4)*, 149–169. https://doi.org/10.1016/j.tecto.2004.02.004

Metropolis, N., Rosenbluth, M.N., Rosenbluth, A.W., Teller, A.H., Teller, E. 1953. Equation of state calculations by fast computing machines. *The Journal of Chemical Physics 21*, 1097–1092.

Monna, S., Montuori, C., Piromallo, C., Vinnik, L. 2019. Mantle structure in the central Mediterranean region from P and S receiver functions. *Geochemistry, Geophysics, Geosystems 20*. https://doi.org/10.1029/2019GC008496

Monna, S., Montuori, C., Frugoni, F., Piromallo, C., Vinnik, L., AlpArray Working Group, 2022. Moho and LAB across the Western Alps (Europe) from P and S receiver function analysis. *Journal of Geophysical Research: Solid Earth 127*, e2022JB025141, https://doi.org/10.1029/2022JB025141

Morais, I.M. 2012. *Structure of the Crust and Mantle Beneath Iberia and Western Mediterranean from P and S Receiver Functions and Sks Waveforms*. Portugal: Universidade De Lisboa, Departamento De Engenharia, Geofisica.

Morais, I., Vinnik, L., Silveira, G., Kiselev, S., Matias, L. 2015. Mantle beneath the Gibraltar Arc from receiver functions. *Geophysical Journal International 200*, 1153–1169. https://doi.org/10.1093/gji/ggu456

Mosegaard, K., Vestergaard, P.D. 1991. A simulated annealing approach to seismic model optimization with sparse prior information. *Geophysical Prospecting 39*, 599–611.

Mosegaard, K., Tarantola, A. 1995. Monte Carlo sampling of solutions to inverse problems. *Journal of Geophysical Research: Solid Earth 100(B7)*, 12431–12447. https://doi.org/10.1029/94JB03097

Mueller, St. 1977. A new model of the continental crust. *The Earth's Crust*: *its Nature and Physical Properties*, edited by Heacock, J.G., *20*, 289–317. AGU, Washington, DC.

Mulumulu, E., Polat, O., Chávez-García, F.J. 2025. 3-D shallow crustal structure and offshore geothermal potential of the Aegean region of Türkiye from ambient noise tomography. *Journal of Asian Earth Sciences 278*, 106–414. https://doi.org/10.1016/j.jseaes.2024.106414

Oreshin, S., Vinnik, L., Peregoudov, D., Roecker, S. 2002. Lithosphere and asthenosphere of the Tien Shan imaged by S receiver functions. *Geophysical Research Letters 29(8)*, 32–1–32–4. https://doi.org/10.1029/2001GL014441

Oreshin, S., Kiselev, S., Vinnik, L., Prakasam, K.S., Rai, S.S., Maketeva, L., Savvin, Y. 2008. Crust and mantle beneath western Himalaya, Ladakh and western Tibet from integrated seismic data. *Earth and Planetary Science Letters 271*, 76–87. https://doi.org/10.1016/j.epsl.2008.03.048

Oreshin, S.I., Vinnik, L.P., Kiselev, S.G., Rai, S.S., Prakasam, K.S., Treussov, A.V. 2011. Deep seismic structure of the Indian shield, western Himalaya, Ladakh and Tibet. *Earth and Planetary Science Letters 307*, 415–429. https://doi.org/10.1016/j.epsl.2011.05.016

Öztürk, S., Alkan, H., 2024. An evaluation of the earthquake potential with seismic and tectonic variables for the West Anatolian region of Türkiye. *Baltica 37(2)*, 110–124. https://doi.org/10.5200/baltica.2024.2.3

Papathoma-Köhle, M. 2025. Letter to the Editor: Latest earthquakes in Santorini reveal the need for a multi-hazard and multi-vulnerability approach to disaster risk reduction. *Nature Hazards 121*, 11215–11220. https://doi.org/10.1007/s11069-025-07246-8

Papazachos, B.C., Karakostas, V.G., Papazachos, C.B., Scordilis, E.M. 2000. The geometry of the Wadati-Benioff zone and lithospheric kinematics in the Hellenic arc. *Tectonophysics 319*, 275–300. https://doi.org/10.1016/S0040-1951(99)00299-1

Reilinger, R., McClusky, S., Vernant, P., Lawrence, S., Ergintav, S., Cakmak, R. 2006. GPS constraints on continental deformation in the Africa-Arabia-Eurasia continental collision zone and implications for the dynamics of plate interactions. *Journal of Geophysical Research 111(B05411)*, 1–26. https://doi.org/10.1029/2005JB004051

Sachpazi, M., Laigle, M., Charalampakis, J., Diaz, E., Kissling, A., Gesret, A., Becel, E., Flueh, Miles, P., Hirn, A. 2016. Segmented Hellenic slab rollback driving Aegean deformation and seismicity. *Geophysical Research Letters 43*, 651–658. https://doi.org/10.1002/2015GL066818

Sachpazi, M., Kapetanidis, V., Laigle, M., Papanikolaou, D., Galve, A., Charalampakis, M., Kissling, E. 2025. Bimodal slip segmentation of the SW Hellenic megathrust revealed by the Mw 6.8 Methoni earthquake sequence and tomography. *Journal of Geophysical Research: Solid Earth 130*, e2024JB030788. https://doi.org/10.1029/2024JB030788

Salaün, G., Pedersen, H.A., Paul, A., Farra, V., Karabulut, H., Hatzfeld, D., Papazachos, C., Childs, D.M., Pequegnat, C., SIMBAAD Team. 2012. High-resolution surface wave tomography beneath the Aegean-Anatolia region: constraints on upper-mantle structure. *Geophysical Journal International 190(1)*, 406–420. https://doi.org/10.1111/j.1365-246X.2012.05483.x

Sardeli, E., Michas, G., Pavlou, K., Vallianatos, F., Karakonstantis, A., Chatzopoulos, G. 2023. Complexity of Recent Earthquake Swarms in Greece in Terms of Non-Extensive Statistical Physics. *Entropy 25*, 667. https://doi.org/10.3390/e25040667

Silveira, G., Vinnik, L., Stutzmann, E., Kiselev, S., Farra, V., Morais, I. 2010. Stratification of the Earth beneath the Azores from P and S receiver functions. *Earth and Planetary Science Letters 229*, 91–103. https://doi.org/10.1016/j.epsl.2010.08.021

Sodoudi, F., Kind, R., Hatzfeld, D., Priestley, K., Hanka, W., Wylegalla, K., Stravrakakis, G., Vafidis, A., Harjes, H.P., Bohnhoff, M. 2006. Lithospheric structure of the Aegean obtained from P and S receiver functions. *Journal of Geophysical Research: Solid Earth 111(B12)*. https://doi.org/10.1029/2005JB003932

Sodoudi, F., Brüstle, A., Meier, T., Kind, R., Friederich, W., Egelados Working Group. 2015. Receiver function images of the Hellenic subduction zone and comparison to microseismicity. *Solid Earth 6(1)*, 135–151. https://doi.org/10.5194/se-6-135-2015

Stemmler, K., Walther, M. 2013. *Seismic Handler Development*. Federal Institute for Geosciences and Natural Resources.

Tamtaş, B.D., Toktay, H.D. 2025. Investigation of Potential Structures in the Southeastern Aegean Region Using Seismological and Gravity Data. *An-*

nals of Geophysics 68(2), DM216–DM216. https://doi.org/10.4401/ag-9229

Tezel, T., Shibutani, T., Kaypak, B. 2013. Crustal thickness of Turkey determined by receiver function. *Journal of Asian Earth Sciences 75*, 36–45. https://doi.org/10.1016/j.jseaes.2013.06.016

Tirel, C., Gueydan, F., Tiberi, C., Brun, J.P. 2004. Aegean crustal thickness inferred from gravity inversion. Geodynamical implications. *Earth and Planetary Science Letters 228(3–4)*, 267–280. https://doi.org/10.1016/j.epsl.2004.10.023

Toyokuni, G., Zhao, D. 2025. Whole-mantle tomography beneath eastern Mediterranean and adjacent regions. *Geophysical Journal International 241(2)*, 1155–1172. https://doi.org/10.1093/gji/ggaf086

Van Der Meijde, M., Van Der Lee, S., Giardini, D. 2003. Crustal structure beneath broad-band seismic stations in the Mediterranean region. *Geophysical Journal International 152(3)*, 729–739. https://doi.org/10.1046/j.1365-246X.2003.01871.x

Vanacore, E.A., Taymaz, T., Saygin, E. 2013. Moho structure of the Anatolian Plate from receiver function analysis. *Geophysical Journal International 193*, 329–337. https://doi.org/10.1093/gji/ggs107

Vinnik, L. 1977. Detection of waves converted from P to SV in the mantle. *Physics of the Earth and Planetary Interiors 15*, 39–45. https://doi.org/10.1016/0031-9201(77)90008-5

Vinnik, L.P. 2019. Receiver Function Seismology. *Izvestya, Physics of Solid Earth 55*, 12–21. https://doi.org/10.1134/S1069351319010130

Vinnik, L., Chevrot, S., Montagner, J. P., Guyot, F. 1999. Teleseismic travel time residuals in North America and anelasticity of the asthenosphere. *Physics of the Earth and Planetary Interiors 116(1–4)*, 93–103. https://doi.org/10.1016/S0031-9201(99)00132-6

Vinnik, L.P., Reigber, C., Aleshin, I.M., Kosarev, G.L., Kaban, M.K., Oreshin, S. I., Roecker, S.W. 2004. Receiver function tomography of the central Tien Shan. *Earth and Planetary Science Letters 225(1–2)*, 131–146. https://doi.org/10.1016/j.epsl.2004.05.039

Vinnik, L.P., Aleshin, I.M., Kaban, M.K., Kiselev, S.G., Kosarev, G.L., Oreshin, S.I., Reigber, Ch. 2006. Crust and mantle of the Tien Shan from data of the receiver function tomography. *Izvestya, Physics of Solid Earth 42*, 639–651. https://doi.org/10.1134/S1069351306080027

Vinnik, L., Oreshin, S., Kosarev, G., Kiselev, S., Makeyeva, L. 2009. Mantle anomalies beneath southern Africa: evidence from seismic S and P receiver functions. *Geophysical Journal International 179*, 279–298. https://doi.org/10.1111/j.1365-246X.2009.04261.x

Vinnik, L., Kozlovskaya, E., Oreshin, S., Kosarev, G., Piiponen, K., Silvennoinen, H. 2016. The lithosphere, LAB, LVZ and Lehmann discontinuity under central Fennoscandia from receiver functions. *Tectonophysics 667*, 189–198. https://doi.org/10.1016/j.tecto.2015.11.024

Wessel, P., Luis, J.F., Uieda, L.A., Scharroo, R., Wobbe, F., Smith, W.H., Tian, D. 2019. The generic mapping tools version 6. *Geochemistry, Geophysics, Geosystems 20(11)*, 5556–5564. https://doi.org/10.1029/2019GC008515

Yolsal-Çevikbilen, S., Taymaz, T. 2012. Earthquake source parameters along the Hellenic subduction zone and numerical simulations of historical tsunamis in the Eastern Mediterranean. *Tectonophysics 536*, 61–100. https://doi.org/10.1016/j.tecto.2012.02.019

Zhu, L., Mitchell, B. J., Akyol, N., Cemen, I., Kekovali, K. 2006. Crustal thickness variations in the Aegean region and implications for the extension of continental crust. *Journal of Geophysical Research: Solid Earth 111(B1)*. https://doi.org/10.1029/2005JB003770